Preliminary Experimental Assessment of the Boundary Layer Ingestion Benefit for the D8 Aircraft

Alejandra Uranga[*], Mark Drela[†], Edward M. Greitzer[‡],
Neil A. Titchener[§], Michael K. Lieu[¶], Nina M. Siu[¶], Arthur C. Huang[‖]

Massachusetts Institute of Technology, Cambridge, MA 02139, U.S.A.

Gregory M. Gatlin[**], Judith A. Hannon[††]

NASA Langley Research Center, Hampton, VA 23681, U.S.A.

Wind tunnel experiments were performed to quantify the aerodynamic benefit of boundary layer ingestion (BLI) for the D8 transport aircraft concept. Two powered 1:11 scale, 13.4 ft span models, in BLI and non-BLI versions, were tested at the NASA Langley 14×22 Foot Subsonic Wind Tunnel to directly compare their performance. The models share the same basic airframe and propulsor units for the most direct comparison. They are also fully tripped to make the measured BLI benefit results scalable to the full-size aircraft. The comparison metric is the propulsor power required to produce a given net stream-wise force on the entire aircraft. The results show that the model BLI propulsors require 6% less electrical power at the simulated cruise point. These experiments provide the first back-to-back assessment quantifying the aerodynamic benefits of BLI for a civil aircraft. The BLI benefit quoted is preliminary in nature because it is defined in terms of electrical power, but we are in the process of obtaining a value in terms of flow power and there is indication that the BLI saving will remain essentially the same.

Nomenclature

c	model reference chord (= 10.75 in = 0.273 m)
C_L	lift (net vertical force) coefficient $= F_Z / (q_\infty \, S_{\text{ref}})$
C_{P_E}	electrical power coefficient $= P_E / (q_\infty \, S_{\text{ref}} \, V_\infty)$
C_{P_K}	mechanical flow power coefficient $= P_K / (q_\infty \, S_{\text{ref}} \, V_\infty)$
C_{p_0}	stagnation pressure coefficient $= (p_0 - p_{0_\infty}) / q_\infty$
C_X	net stream-wise force coefficient $= F_X / (q_\infty \, S_{\text{ref}})$ ($= C_D$ for unpowered configuration)
D	model propulsor fan diameter (= 5.65 in = 0.144 m)
F_X	net stream-wise force on model; negative values indicate net thrust
F_Z	net vertical (normal to tunnel free-stream direction) force on model
M_∞	free-stream (tunnel) Mach number
p_0	stagnation pressure
p_{0_∞}	free-stream (tunnel) stagnation pressure
P_E	electrical power supplied to propulsors

---

[*]Research Engineer, Dept. of Aeronautics and Astronautics, 77 Massachusetts Avenue Room 31-268, Cambridge, MA 02139, auranga@mit.edu, AIAA Member.

[†]Terry J. Kohler Professor of Fluid Dynamics, Dept. of Aeronautics and Astronautics, AIAA Fellow.

[‡]H.N. Slater Professor of Aeronautics and Astronautics, Dept. of Aeronautics and Astronautics, AIAA Honorary Fellow.

[§]Postdoctoral Associate, Dept. of Aeronautics and Astronautics, AIAA Member.

[¶]Graduate Student, Dept. of Aeronautics and Astronautics, AIAA Member.

[‖]Research Engineer, Dept. of Aeronautics and Astronautics

[**]Senior Research Engineer, Configuration Aerodynamics Branch, Mail Stop 267, AIAA Senior Member.

[††]Aerospace Engineer, Flow Physics and Control Branch, Mail Stop 170.

American Institute of Aeronautics and Astronautics

P_K mechanical flow power

q_∞ free-stream (tunnel) dynamic pressure $= \frac{1}{2}\,\rho_\infty\,V_\infty^2$

Re_c Reynolds number based on reference chord and free-stream (tunnel) conditions

S_ref model reference area ($= 1686$ in$^2 = 1.088$ m^2 at 1:11 scale)

U_tip fan blade tip speed $= \Omega\,D\,/2$

V_∞ free-stream (tunnel) speed

x, y, z model axes: x is longitudinal, y is span-wise

X, Y, Z tunnel axes: X is stream-wise (horizontal direction) and Z is vertical

α model angle of attack with respect to tunnel free-stream X direction

$\Delta(\ )$ repeatability of quantity

η_m motor efficiency $= P_\mathrm{shaft}\,/\,P_E$

η_f fan efficiency $= P_K\,/\,P_\mathrm{shaft}$

σ measurement uncertainty

Ω fan angular velocity, wheel speed

I. Introduction

IN 2008, NASA put forward a solicitation for aircraft concepts targeted for three generations ahead of the current flying fleet. This "N+3" program aims to develop advanced concepts, plus enabling technologies, to provide step improvements in fuel efficiency and lowering the environmental impact of commercial aircraft entering service in the 2025-2035 timeframe. During Phase 1 of the N+3 program[a], a team led by MIT, in partnership with Aurora Flight Sciences and Pratt & Whitney, developed a conceptual design for a 180-passenger, 3 000 nm range transport, in the Boeing 737 or Airbus A320 aircraft class. This so-called D8 *double-bubble* aircraft (named for its characteristic double bubble fuselage cross-section) was estimated to require 71% less fuel while generating 76% fewer emissions (LTO NOx) than the 737-800 used as the basis for comparison.[1]

In Phase 2 of the program[b], the team is advancing the D8 concept through high-fidelity computations and through wind tunnel experiments. This involves the detailed aerodynamic design of the integrated fuselage and propulsion system, as well as development of suitable scaling arguments, metrics, and baselines for experimental BLI evaluation. A major component of this work is a series of experiments in NASA Langley's 14×22 Foot Subsonic Wind Tunnel using 1:11 scale, 13.4 ft span, powered models to evaluate the aerodynamic performance both with and without BLI. A picture taken during the first set of tests undertaken in August–September 2013 is shown in Figure 1. The performance metric used to quantify the aerodynamic BLI benefit is the power required to produce a given net stream-wise force on the aircraft.

Figure 1. D8 model in BLI integrated configuration in NASA Langley's 14×22 wind tunnel during the August–September 2013 experiments (photo credit NASA/George Homich).

Three configurations of the D8 were tested in August and September 2013: (i) an unpowered model to characterize the airframe alone, (ii) a model with conventional nacelle, power by podded propulsors which ingest free-stream flow to serve as the baseline, and (iii) an integrated aircraft model whose propulsors are flush-mounted above the rear of the fuselage and ingest part of the fuselage boundary layer. To remove extraneous variability and facilitate comparison between the BLI and non-BLI configurations, the three versions share components and propulsion units to a high degree. The focus of this first set of tests was the

---

[a]September 2008 through March 2010

[b]November 2010 through November 2014

American Institute of Aeronautics and Astronautics

simulated cruise condition. Other conditions, including high angle of attack and deep stall, high yaw, and engine-out, are being considered for future tests.

These experiments advance the technology-readiness level of the full-size D8 aircraft concept for the following reasons. First, the applicability of sub-scale tests to large scales drives experimental choices. For example, the non-dimensional fan disk loadings and propulsive efficiencies in this experiment are representative of full-size aircraft. Second, the combination of large model size and appropriate boundary layer trips on all surfaces ensure turbulent flow, so that the results can be scaled to full-size aircraft Reynolds numbers. Third, the model is large enough for performing detailed flow-field measurements of propulsor inflows and outflows. Fourth, the use of electrical motors allows direct measurement of the flow power input for use as a surrogate for fuel burn. Finally, the high quality of the flow and force measurements in the 14×22 tunnel ensure accurate resolution of the aerodynamic differences between non-BLI and BLI configurations.

The scope of the paper is as follows. We first present an overview of the D8 aircraft concept, followed by a description of boundary layer ingestion and the metrics used to assess its effects. A description of the experiment is then provided, including features of the different model configurations, description of the wind tunnel, the experimental procedures, and the uncertainty and repeatability in the measurements. Vehicle performance results are shown, the most important of these being the 6% decrease in power needed by the propulsors at the simulated cruise condition with BLI compared to the non-BLI configuration. Interesting features of the BLI propulsor inlet flow, which influence propulsor operation, are also shown. The paper concludes with a summary of the most important learning from this first set of experiments and a brief discussion of the next steps in the Phase 2 program.

II.   The D8 Aircraft Concept

The D8 configuration[2] is characterized by a wide twin-aisle lifting fuselage producing close to 19% of the aircraft's total lift (compared to 13% for a 737-800) which enables the use of smaller and lighter wings and a pi-tail with a two-point structural support. The fuselage nose shape also provides a positive nose-up pitching moment of roughly $+0.084$ in C_M, which reduces the required horizontal tail size. It also reduces the trimming tail down-force in cruise by $+0.03$ in C_L, thus shrinking the wing area. A low-sweep wing contributes to a lighter structure and is made possible by a cruise speed of Mach 0.72, compared to Mach 0.80 for the 737-800 aircraft. Numerous additional features contribute to a significant overall fuel-burn reduction.

For the present work, the most important feature of the D8 configuration is that it allows the engines to be flush-mounted on the top rear of the fuselage, which ingest roughly 40% of the fuselage boundary layer[c]. The engines are located near the fuselage's rear stagnation point, so that the fuselage performs much of the diffusion and flow alignment into the fans which is normally performed by the nacelle of an isolated podded engine. As a result, the D8 nacelles are smaller, saving considerable weight and reducing external wetted-area losses. This engine placement also enables a shorter and lighter landing gear, and allows the fuselage to provide noise shielding.

The design features described above are the key characteristics of the D8.2 aircraft concept shown in Figure 2. Compared to the equivalent 737-800, the D8.2 achieves a 36% reduction in fuel burn from the configuration alone, without resorting to advanced materials or advanced engine-core technology. During Phase 1 of the N+3 effort, additional technological advances expected to occur in the next 20–30 years were predicted to yield fuel burn savings close to 71% relative to the 737-800,[1] and are exemplified by the D8.6 aircraft concept. The focus of Phase 2 and this paper is entirely on BLI, one of the enabling technologies for the D8.2 aircraft which could enter service in a shorter term.

During the Phase 1 study, the D8 BLI engine installation was designed at the conceptual level only, and hence its advantages have been largely theoretical. Because the geometry near the engines is complex, and includes integration with the rear fuselage and the twin vertical tails, the possibility of unexpected interference losses was always present. A major goal of the Phase 2 effort therefore is to perform a detailed aerodynamic design of this installation, and evaluate its performance both experimentally and computationally to demonstrate that such a configuration can be realized without unexpected aerodynamic losses.

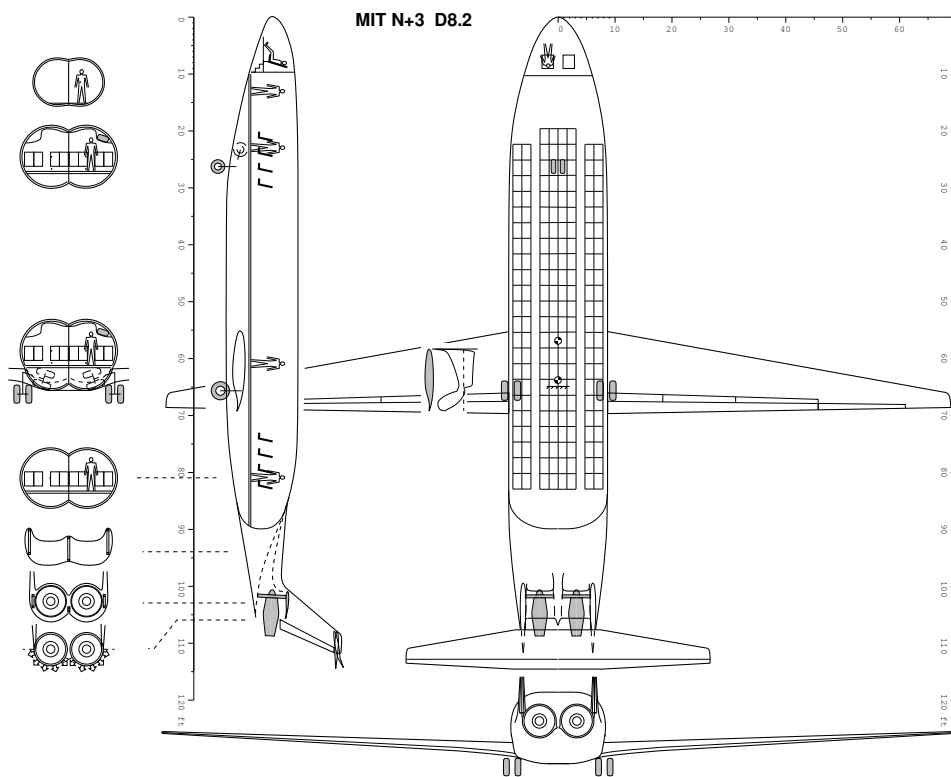[c]as computed based on fuselage kinetic energy defect in the complementary CFD study[3]

American Institute of Aeronautics and Astronautics

Figure 2. Three-view of D8.2 transport aircraft concept.

III. Performance Metrics for Boundary Layer Ingestion

A. BLI analysis

The theoretical benefit of boundary layer ingestion (BLI) on propulsive efficiency is well established, and has been analyzed using a number of different frameworks. The classical explanation dating back to Betz[4] is that a reduced inflow velocity of the propulsive stream-tube results in less power being required to impart a given momentum flow to the stream-tube. This approach was used by Smith,[5] whose analysis suggested that power savings as large as 50% were possible for some combinations of inflow wake profiles and high propulsor disk loadings. For more practical disk loadings the savings were estimated to be a more modest 10% − 20%.

An alternative view of BLI as analyzed by Drela[6] is that it reduces the power dissipation in the overall flowfield, primarily by reducing the stream-wise velocities and associated wasted kinetic energy left by the aircraft by "filling-in" the wake with the propulsor, as sketched in Figure 3. One advantage of this power balance approach is that it unifies all the power losses on the aircraft, both surface boundary layer losses of the airframe and the propulsive losses of the power plant, without the need to resort to drag and thrust estimation. Indeed, one practical complication of BLI is that although the total stream-wise force is well-defined, its decomposition into "drag" and "thrust" components is ambiguous. This is true even for non-BLI configurations where the airframe and propulsor pressure fields interact, although the ambiguity is especially severe in the case of BLI. In the power-balance framework, the design objective is then not to minimize engine power for a required thrust (equal to airframe drag), but rather to minimize engine power needed to produce a zero net stream-wise force on the overall integrated airframe-propulsion system configuration. The engine thrust force and the airframe drag force do not need to be treated separately or even defined.

The theoretical benefit of BLI is likely to be mitigated to some extent by the unfavorable effect of the distorted propulsor inflow on the fan performance, with the effect depending on fan-blade Mach number, and also on the Reynolds number to some extent. Since the N+3 experiments do not match the Mach or Reynolds numbers, it is necessary here to separate out the fan-efficiency effect from the propulsive-efficiency

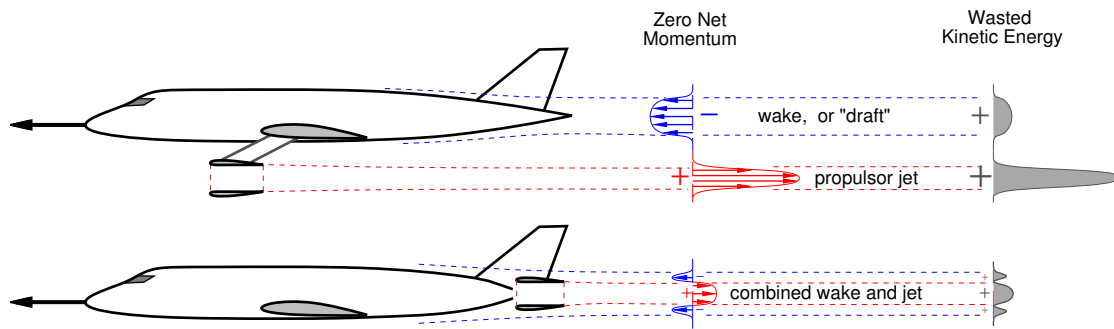American Institute of Aeronautics and Astronautics

Figure 3. Illustration of power-saving benefit of boundary layer ingestion (bottom) compared to a conventional aircraft (top). Reduction in axial wake velocities of combined wake and jet results in a reduction in wasted kinetic energy deposited in the flow.

effect, which is conveniently done using the power-balance framework of Drela.[6]

The three types of mechanical power sources within a flowfield are net mechanical power P_K across propulsor inflow and outflow planes, shaft power P_S from moving surfaces, and volumetric "p dV" work P_V within the flowfield, as described by Drela.[6] For the control volume chosen here which fully envelopes the propulsor, and in the low speed case, the sole remaining flowfield power source P_K is then given by the volume flux of total pressure

$$P_K = \oiint (p_{0_\infty} - p_0) \, \mathbf{V} \cdot \hat{\mathbf{n}} \, \mathrm{d}S \; . \tag{1}$$

The area integral is taken over the inflow and outflow planes of the propulsor, so that P_K is a measure of net engine flow power, and any losses internal to the propulsor are immaterial. This then separates the issue of fan efficiency from the aerodynamics of the BLI configuration, and the fan blading losses due to BLI can then be accounted for separately.

B. BLI performance parameters

This section defines and discusses the various parameters used to quantify and evaluate the performance of the BLI system in this experiment.

1. Net horizontal force coefficient

In a BLI system the thrust and drag forces are ambiguous, so we use only the net stream-wise force F_X, or "drag − thrust," which is always well-defined. Its non-dimensional form is the stream-wise force coefficient

$$C_X \equiv \frac{F_X}{q_\infty \, S_{\mathrm{ref}}} \; .$$

2. Net propulsor power coefficient

In the experiment P_K can be measured by surveying the propulsor inflow and outflow planes by the rotating total and static rake system shown in Figure 12. The velocity magnitudes in this incompressible flow are then obtained from total and static pressure distributions. This velocity, together with an assumed flow direction and the measured total pressure, is used to calculate P_K from its definition (1) by appropriate numerical integration. The result is then non-dimensionalized into the corresponding flow power coefficient

$$C_{P_K} \equiv \frac{P_K}{q_\infty \, V_\infty \, S_{\mathrm{ref}}} \; .$$

American Institute of Aeronautics and Astronautics

3. Electrical power coefficient

An alternative way to obtain the propulsor power P_K is via the measured electrical power P_E supplied to the motor, together with motor and fan efficiencies η_m and η_f which can be measured in separate off-line experiments. The electrical power coefficient is defined as

$$C_{P_E} \;\; \equiv \;\; \frac{P_E}{q_\infty \, V_\infty \, S_{\mathrm{ref}}} \;, \tag{2}$$

and the two power coefficients are related through

$$C_{P_K} \;\; = \;\; \eta_f \, \eta_m \, C_{P_E} \;. \tag{3}$$

The advantage of using this relation to obtain C_{P_K} is that electrical motor power can be measured reliably and instantly, in contrast to the flow survey method which is relatively time consuming. The disadvantage of using (3) is that uncertainties in the off-line measurements of the motor and fan efficiencies introduce additional uncertainties in the resulting C_{P_K} values.

4. BLI benefit

The primary objective of BLI is to reduce the propulsor flow power required to achieve a net stream-wise force on the aircraft. The aerodynamic BLI benefit can therefore be expressed as

$$\mathrm{BLI\ benefit} \equiv \frac{(C_{P_K})_{\mathrm{non\text{-}BLI}} - (C_{P_K})_{\mathrm{BLI}}}{(C_{P_K})_{\mathrm{non\text{-}BLI}}} \;. \tag{4}$$

As mentioned above, for these preliminary results electrical power is used as a surrogate for the flow power, since the former was directly measured during the wind tunnel tests. The aerodynamic BLI benefit (or BLI benefit for short) is taken to be the saving in electrical power

$$\mathrm{BLI\ benefit} \simeq \frac{(C_{P_E})_{\mathrm{non\text{-}BLI}} - (C_{P_E})_{\mathrm{BLI}}}{(C_{P_E})_{\mathrm{non\text{-}BLI}}} \;. \tag{5}$$

Using C_{P_E} to measure BLI benefit is justified if the efficiencies η_f and η_m do not change significantly between the podded and integrated installations at same operating point. Initial fan and motor efficiency measurements indicate that the fan operates mostly within its loss bucket for the two configurations, and that the motor is close to its peak efficiency. Therefore, (5) is a good substitute for (4), and hence C_{P_E} is used throughout this paper.

Supplemental experiments are underway to precisely measure the fan and motor efficiencies, and thus eliminate any uncertainties introduced by the assumption of constant efficiencies. They will allow us to quantify the BLI benefit in terms of flow power rather than electrical power, and the results will be presented in a follow-up paper.

5. Bases of comparison of BLI and non-BLI configurations

Given a BLI propulsor with some jet velocity, mass flow, and nozzle area, there is no unique way to choose an "equivalent" non-BLI propulsor as a basis for comparison. One definite constraint is that the net force (momentum flow) be the same. However, this is not sufficient; the mass flow must also be constrained in some manner, typically via the nozzle area which can be thought of as a surrogate for propulsive efficiency—as nozzle area increases, jet velocity decreases and hence propulsive efficiency increases. Each different nozzle area therefore results in a different non-BLI baseline propulsor mass flow and performance, and a different BLI benefit value.

Specific choices are to make the comparison at equal mass flow, equal nozzle area, equal jet velocity, or equal power. The BLI benefit is manifested differently for each of these comparisons as illustrated in Figure 4. For example, at constant nozzle area, the non-BLI configuration requires roughly 7% more propulsive power. At the other extreme, the non-BLI propulsor which requires the same amount of power requires a much larger nozzle which would impose a system-level weight penalty.
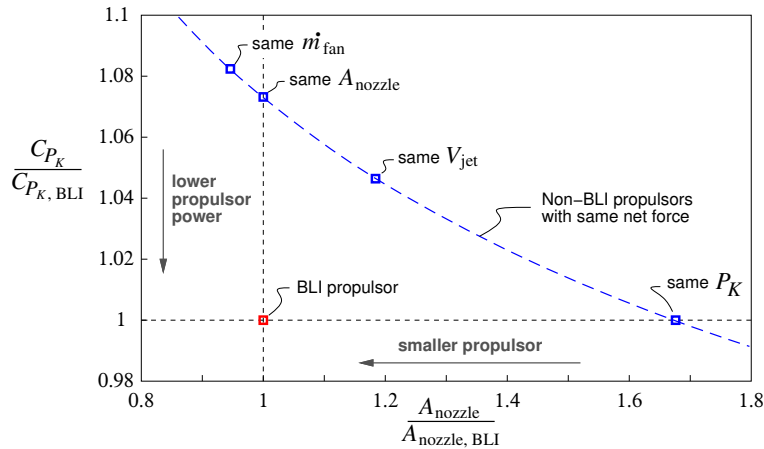
American Institute of Aeronautics and Astronautics

Figure 4. Non-BLI propulsor power relative to BLI propulsor, versus nozzle area at zero stream-wise force.

Another benefit of BLI, which is not represented in Figure 4, is the reduction of external nacelle losses. On conventional engine installations the nacelle aligns the inflow with the engine axis, and also diffuses the inflow to $M \simeq 0.6$ which is what's required by a typical fan. On the D8 installation these functions are performed mainly by the rear fuselage, allowing the D8 nacelles to be minimal in thickness (see Figure 8). The D8 nacelles also cover only the upper half of each fan, and have surface velocities lower than the free-stream. Consequently their viscous losses are only about a quarter of those for a conventional nacelle.[2]

The goal of this study is to quantify the *aerodynamic* benefit of BLI, which we define as consisting of: the propulsive benefits of reducing jet and wake losses; and the external aerodynamic benefits resulting from reducing external nacelle surface friction losses. We therefore choose to use propulsors with equal nozzle areas, and actually the same physical propulsors, on the non-BLI and BLI D8 configurations. The nacelles for each configuration are also designed for minimum external losses for the most relevant and fair back-to-back comparison. However, to put the results of the present study in the overall airplane-design context, additional system-level aerodynamic and weight benefits which are enabled by adopting a BLI propulsion system must also be considered, as discussed next.

C. System Impact of BLI

To quantify all the benefits of BLI, including those at the system level, a sequence of conceptual aircraft designs are defined and optimized using the TASOPT methodology,[1].[2] This also quantifies the system-level benefits of the D8 fuselage which allows the engines to be flush-mounted on the top rear fuselage and ingest its boundary layer.

Starting with the baseline 737-800 aircraft, the distinctive design features of the D8 are introduced one at a time, and each design is optimized to minimize mission fuel burn. This results in a sequence through which the 737-800 "morphs" into the D8.2 aircraft, with the fuel burn for each design step shown in Figure 5. The parameter changes which occur at each step can then be examined to determine the physical origin of fuel burn reduction benefits, including the system-level effects.

The main design variables optimized at every step of this process are cruise C_L, wing aspect ratio AR, wing sweep angle, airfoil thickness-to-chord ratio at several span-wise stations, span-wise load distribution, turbofan combustor temperatures T_{t4} at takeoff and cruise, and the start-of-cruise altitude h_{cruise}. The key aircraft parameter values as they evolve over the morphing sequence are listed in Table 1.

The morphing process starts from a version of the 737-800 optimized with TASOPT at step 0. The first morphing step from design 0 to 1 is the result of slowing down the cruise speed from Mach 0.80 to 0.72, which gives fuel burn reduction mainly from a larger aspect ratio and a larger cruise C_L, both enabled structurally and aerodynamically by a smaller sweep. The change to the D8 double-bubble fuselage from case 1 to 2 reduces fuel burn mainly from a reduced maximum weight, which is due to the larger fuselage lift fraction and nose-up pitching moment offset. The bypass ratio (BPR) and fan pressure ratio (FPR) are for now held fixed at the values of the CFM56 engine used on the 737-800.

American Institute of Aeronautics and Astronautics

Table 1. Optimized aircraft parameters in "morphing" redesign study. The combustor T_{t4} is at cruise.

Step	M cruise	BLI?	W_{max} (lb)	W_{fuel} (lb)	Span (ft)	S (ft^2)	AR	Sweep (deg)	C_L	h_{cruise} (ft)	T_{t4} (K)	BPR	FPR	OPR
0	0.80	N	160858	35131	115.8	1240	10.8	26.7	0.564	34784	1294	5.100	1.650	30
1	0.72	N	159294	30682	148.9	1338	16.6	11.1	0.677	36110	1233	5.100	1.650	30
2	0.72	N	141850	28518	133.6	1123	15.9	12.0	0.717	36037	1239	5.100	1.650	30
3	0.72	N	144290	28898	143.2	1187	17.3	13.3	0.691	36083	1263	5.100	1.650	30
4	0.72	Y	128852	23517	131.6	1029	16.8	13.1	0.705	35795	1237	5.100	1.650	30
5	0.72	Y	130480	23296	131.0	1033	16.6	12.0	0.711	35769	1419	7.136	1.638	30
6	0.72	Y	129239	22422	132.1	1060	16.5	11.8	0.711	36584	1451	7.704	1.601	40
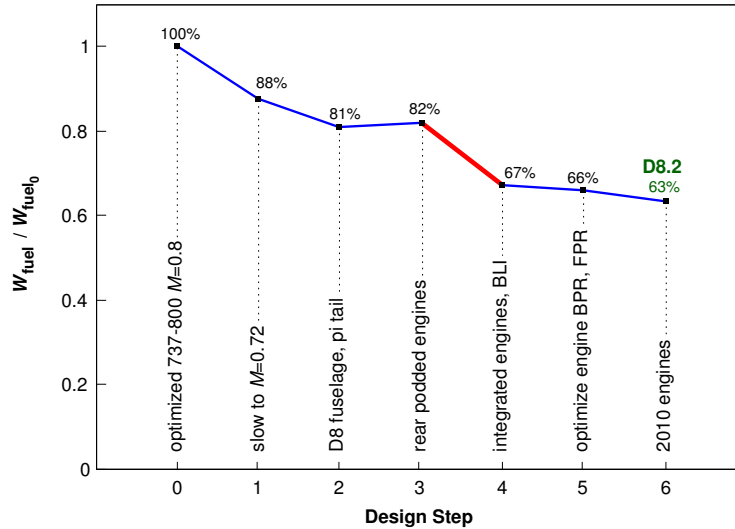
Figure 5. "Morphing" sequence of design changes from the optimized 737-800 baseline (step 0) to the D8.2 configuration (step 6). The vertical axis and percent numbers give the changes in fuel burn with respect to the step 0 baseline. BLI is introduced between steps 3 and 4 (red segment).

The change from step 2 to step 3 is the movement of the engine nacelles from under the wing to the rear of the fuselage. The rearward weight shift increases the tail size, but this is partly offset by the nacelles providing some pitch stability. The maximum engine-out yaw moments are reduced by the slightly smaller engine spacing, and the landing gear is shortened and lightened significantly. Overall, a 1% fuel burn increase is predicted, although this has some uncertainty due to the large degree of cancellation between the numerous competing effects.

BLI is introduced between steps 3 and 4, and consists of moving the rear podded engines to the top of the fuselage. The engine bypass ratio and fan pressure ratio are held fixed for now, but the entire aircraft is re-sized and re-optimized. This gives a fuel burn reduction of about 15%, which is about twice the propulsion-only benefit of 7% predicted by the simplified analysis of the previous section. The extra 8% benefit includes the savings from the reduced nacelle drag, reduced nacelle weight, reduced vertical tail size allowed by the smaller engine-out yaw moments, plus the compounding effect on the overall weight.

Additional benefits of about 1% are produced when the engine parameters are optimized in the presence of BLI from step 4 to step 5. Finally, the 3% reduction between steps 5 and 6 is due to switching to modern 2010 engine technology instead of the 1975 technology of the CFM56. Specifically overall pressure ratio (OPR) is increased from 30 to 40, and the engine weight model is adjusted.

In the present experiment, the BLI and non-BLI cases have essentially the same geometry, so the measured BLI benefit is only due to propulsive and direct aerodynamic effects. However, the morphing study presented here indicates that significantly larger overall benefits can be expected when BLI is incorporated into an optimized aircraft, and BLI is an enabler of these additional benefits.

American Institute of Aeronautics and Astronautics

IV.   Tested Configurations

The present experiment seeks to measure the aerodynamic benefit of BLI for the D8 aircraft, by comparing the performance of two 1:11 scale[d] powered wind tunnel models representative of the full-size D8. The *podded configuration* model, shown in Figure 9, has propulsors on rear-mounted pods which ingest uniform free-stream (clean) flow. This serves as the control case for conventional or non-BLI propulsion. The *integrated configuration* model, shown in Figure 10, has the same physical propulsors but they are embedded into the aft top fuselage to ingest part of the fuselage's boundary layer. A third *unpowered configuration* model, shown in Figure 7, was also tested. It is the same as the podded configuration, except that the propulsor pods are removed. It was used to measure the aerodynamic characteristics of the airframe alone to allow a more complete characterization of the aircraft.

A.   Common Geometry

The unpowered, podded, and integrated models share the same physical components, except for the removable aft 20% of the fuselage and attached vertical tails—the horizontal tail is common. The front fuselage and wing geometry were defined during the Phase 1 work,[1,2] and a 1:11 scale model of the D8.2 is used for this experimental investigation. The schematic in Figure 6 illustrates the model's fuselage cut location aft of which the tails of the podded and integrated configurations differ. Table 2 gives size characteristics of the 1:11 scale models.

Following usual procedures in sub-scale testing, all the model components are tripped to obtain turbulent flow—wings, fuselage, tail surfaces, and propulsor nacelles. The surface trips consisted of 0.125 in wide masking tape in several layers, for a total thickness of 0.018 in on the fuselage and 0.013 in on all other surfaces. Adequacy of the trips was determined by tracking the drag of the unpowered configuration as the thickness of the trip strips was gradually increased (adding layer after later of tape). As the thickness is increased, the initial drag coefficient changes were significant, and the process was stopped once these changes became negligible. Further confirmation of the adequacy of the trips was obtained by comparing drag at different tunnel speeds: decreasing drag is observed with increasing Reynolds number over most of the angle of attack range, as expected when boundary layers are turbulent.

B.   Unpowered Configuration

The unpowered configuration, shown in Figure 7, consists of the D8 common-body and the tail utilized by the podded configuration with no pylons nor propulsors.

The tail section was designed to minimize flow acceleration under the pi-tail (between the verticals) and to keep the rear of the fuselage unloaded as the D8 concept calls for. Care was also taken to unload the verticals when the model faces the flow (zero yaw). This was achieved by toeing out[e] the lower (root) profile of the vertical tails by 3° and toeing out the upper (tip) profile by 1.5°.

---

[d]nominally, the actual scale being 1:11.16
[e]angle between fuselage longitudinal direction and airfoil chord

Table 2. Reference dimensions of the 1:11 D8 models.

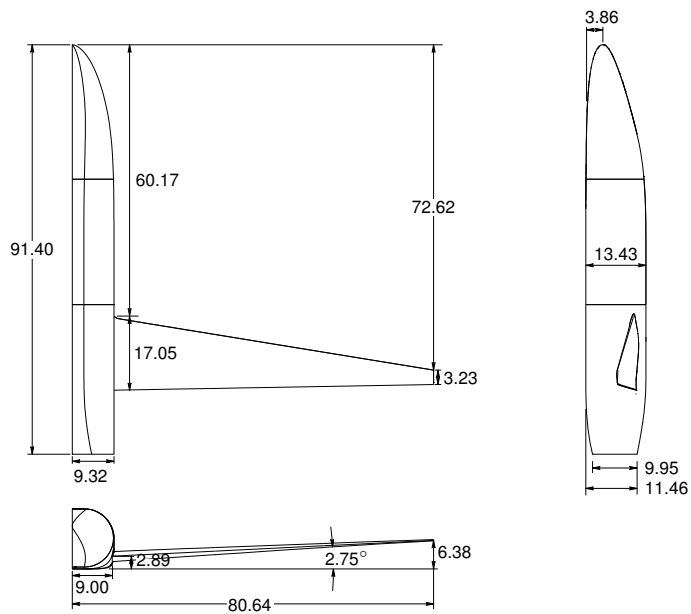| Dimension	Value	
Reference area S_{ref}	1.088 m²	1686.00 in²
Reference chord c	0.273 m	10.75 in
Span	4.097 m	161.3 in
Overall length (podded)	3.218 m	126.69 in
Overall length (integrated)	3.138 m	123.55 in
Propulsor fan diameter	0.144 m	5.65 in

American Institute of Aeronautics and Astronautics

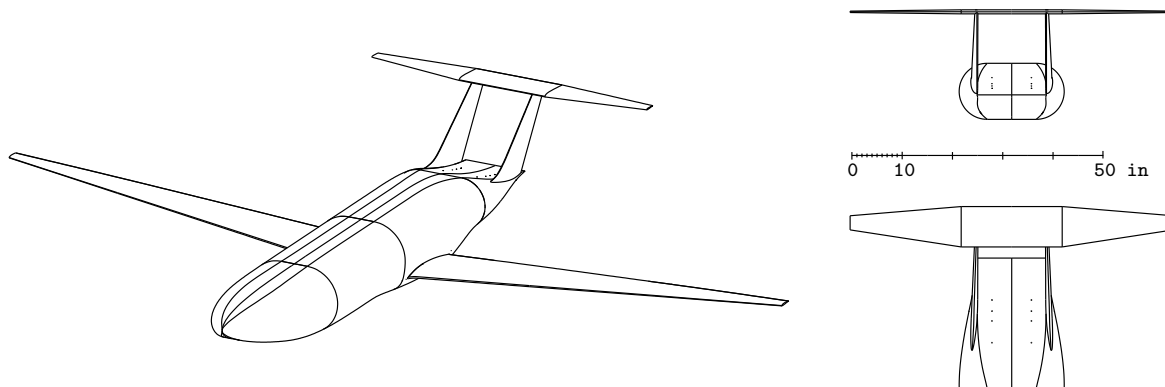**Figure 6. Model geometry common to all configurations. Units: inches.**

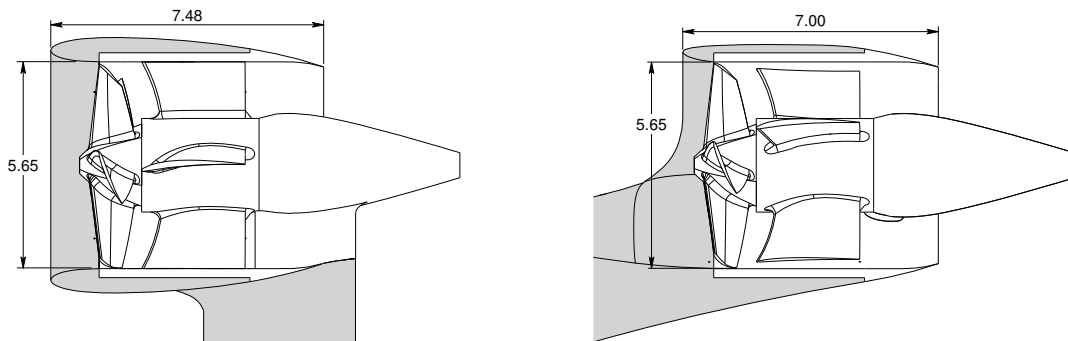**Figure 7. Unpowered configuration geometry.**

Figure 8. Podded (left) and integrated (right) model propulsors. The un-shaded parts are common to both model configurations, and the grayed regions show the nacelles and support structures specific to each configuration. Units: inches.

C. Electric Propulsors

Both podded and integrated configurations are powered by the same two propulsor units, each consisting of a fan stage (rotor and stator), motor, center-body, aluminum housing, nozzle, and power electronics. Using the same propulsor units largely removes variability of the propulsion elements between the two configurations, and thus gives the best possible evaluation of the benefits of BLI alone, separate from any extraneous effects.

Commercially available off-the-shelf fan stages are used, namely carbon-composite TF8000 ducted fans manufactured by Aeronaut primarily for use on RC airplanes. The 5.65 in diameter rotor has 5 blades, and the stator 4 blades. Each propulsor has a 2 kW Lehner Motors 3040-27 brushless DC electric motor. Each motor and its controller is powered by a Sorenson 2 kW DC power supply with a 240 V, 3-phase, input.

The propulsors were designed such that the rotor, stator, internal ducting, center-body, nozzle, and motor comprise a removable piece separate from the outer nacelle, which can then be interchanged between the podded and integrated configuration. Furthermore, each physical propulsor unit had a designated side (on the model's left or right side) and was utilized exclusively on that side throughout the investigation. Figure 8 shows the propulsors with the podded or integrated support nacelle structure indicated in gray.

D. Podded (Non-BLI) Configuration

The podded, or non-BLI, configuration has the propulsor units embedded in nacelles, which are mounted on pylons at the very rear of the aircraft as shown in Figure 9. The length of the pylon and angle at which it intersects the fuselage were chosen to minimize interference between the propulsor and the body. The intent is to make this installation represent an "isolated" propulsion system to serve as a control case to which the BLI installation can be compared.
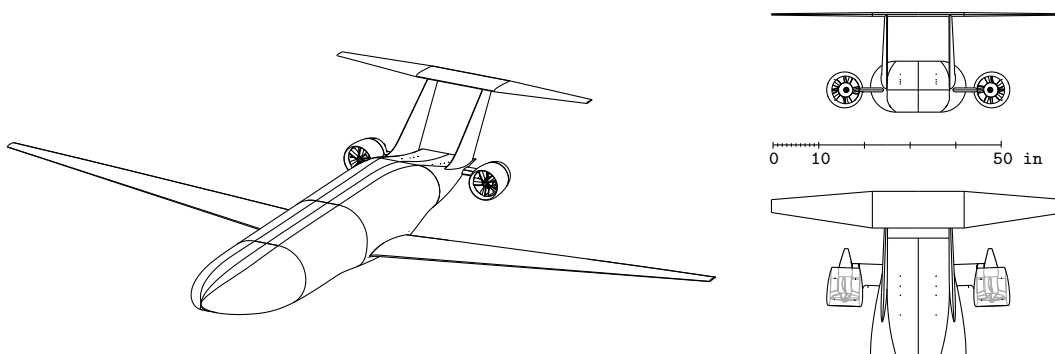

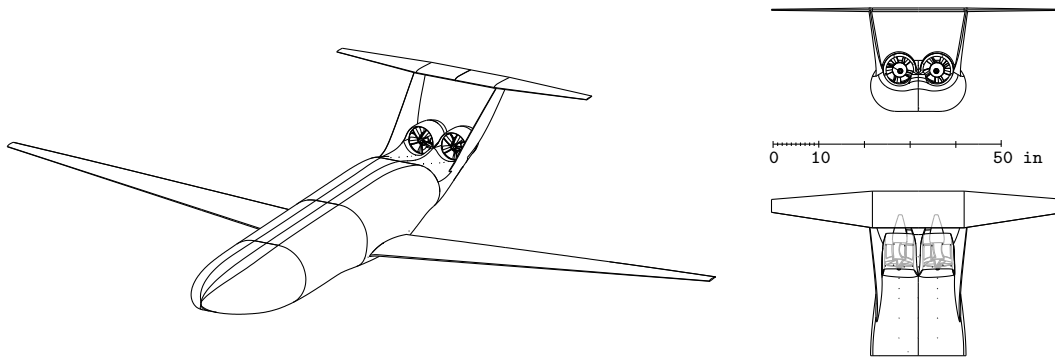
Figure 9. Podded configuration model geometry.

American Institute of Aeronautics and Astronautics

Figure 10. Integrated configuration model geometry.

E.   Integrated (BLI) Configuration

The integrated, or BLI, configuration has the propulsor units embedded in the rear fuselage which also functions as nacelles, and can be seen in Figure 10. The whole fuselage rear (upper and lower surfaces), vertical tails, and propulsor nacelles were designed together as a blended system that provides the required diffusion upstream of the fan while minimizing losses[f].

The vertical tails differ in twist distribution from the podded configuration, in order to align them with the local flowfield of the rear fuselage-propulsion system combination. The nacelles over the integrated propulsors are minimal, with a smaller thickness and leading edge overhang than the podded nacelles as can be seen in Figure 8. The general aerodynamic design objective of the integrated rear fuselage was to obtain a positive pressure coefficient, and zero, or weak, stream-wise pressure gradients over the propulsor nacelles. This minimizes skin friction losses, and also eliminates the need for fillets in the relatively tight inside corners between the two nacelles and especially between the nacelles and the vertical tails.

V.   Experimental Approach

A.   Wind Tunnel

Measurements were conducted in the 14×22 Foot Subsonic Wind Tunnel at the NASA Langley Research Center operating in closed test section mode. The test section has a rectangular cross-section of 14.5×21.75 ft[g]. Figure 11 shows a schematic of the model inside the tunnel. It is mounted on a pitch-head and trunnion system to which the model is attached near the wing's quarter chord and which controls angle of attack as well as model height.

The model is vertically positioned so that a reference point near the wing root is held at the center of the tunnel as the angle of attack is changed. The uncertainty on model position within the test section (vertically and span-wise) is ±1 in. At zero angle-of-attack, the 1:11 scale D8 model results in a wind-tunnel blockage[h] of approximately 0.5%.

B.   Test Procedures

The majority of the tests were performed at the tunnel speed of 70 mph, or Mach 0.092. Two other speeds were used to evaluate Reynolds numbers effects: 42 mph and 56 mph. The reference quantities for these speeds are listed in Table 3. Throughout this document, the terms free-stream, or tunnel, velocity are used to refer to the uncorrected test section velocity provided by the facility's system.

The common body of the D8 was mounted on the trunnion via an internal force balance at the beginning of the four week test program and was not removed until the conclusion of the test—changes between the

---

[f]The integrated aft fuselage and tail design tested during this first set of experiments is not final, and constitutes only a milestone in the complex design process of a D8 aft end. The design will be further refined for future tests.

[g]The tunnel sidewalls slightly diverge, resulting in a width of 21.98 ft at the test section exit 50 ft downstream.

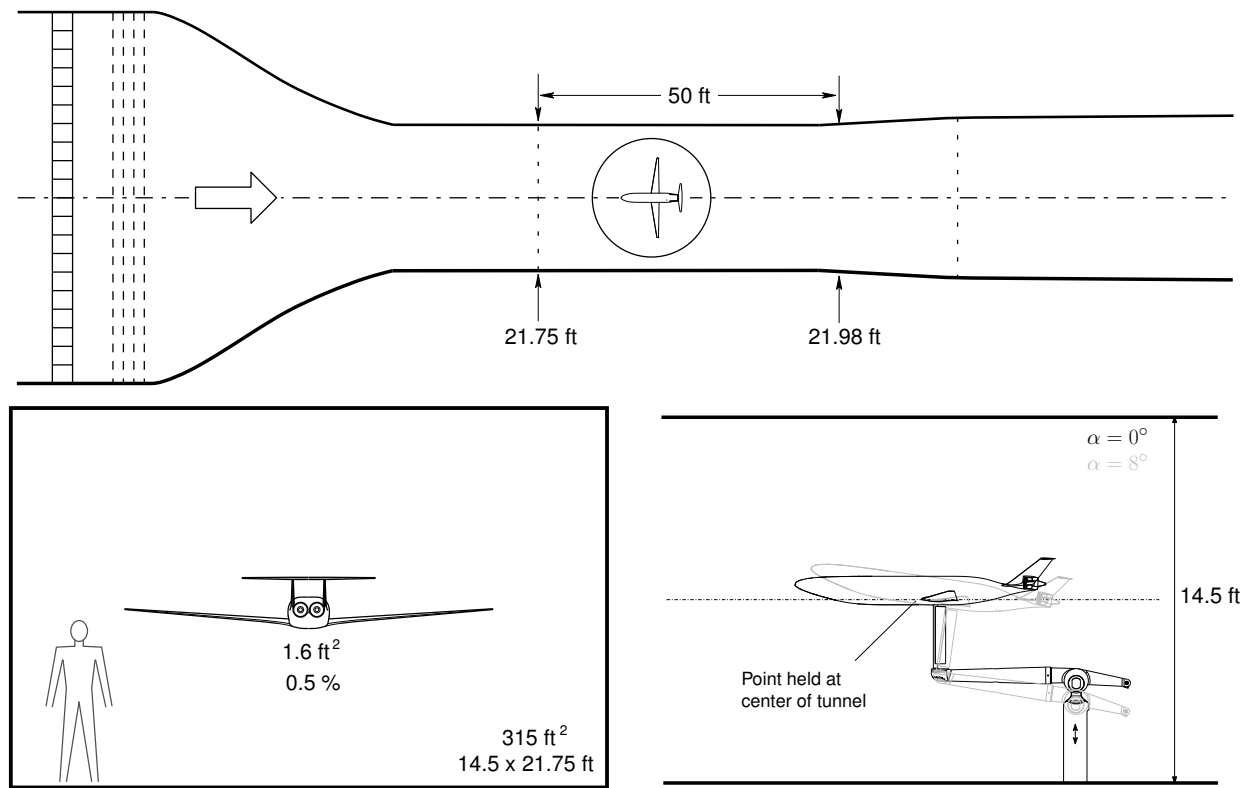[h]Ratio of model to test section cross-sectional areas

American Institute of Aeronautics and Astronautics

Figure 11. Schematic views (top, rear, side) of the D8 model in the test section of NASA Langley's 14×22 tunnel (top view adapted from Ref. 7).

Table 3. Tunnel nominal operating conditions (assuming standard sea level operation).

V_∞		q_∞		M_∞	Re_c
(mph)	(m/s)	(Pa)	(psf)		
42	18.8	216	4.5	0.055	3.6×10^5
56	25.0	382	8.0	0.074	4.6×10^5
70	31.3	598	12.5	0.092	5.7×10^5

Table 4. Propulsor fan wheel speeds tested during each power-sweep run, for $V_\infty = 70$ mph.

Ω (RPM)	5 250	8 000	10 600	12 250	13 500	14 500
U_{tip}/V_∞	1.27	1.93	2.55	2.95	3.25	3.50

American Institute of Aeronautics and Astronautics

unpowered, podded, and integrated configurations were undertaken in situ. When in a powered configuration, the center of gravity of the model is located approximately 5 in aft of the force balance reference center.

After any configuration change, a load-check was performed to verify the model instrumentation, in particular to rule-out any fouling between metric and non-metric components. Weight tares, or wind-off force readings, were obtained before and after every set of runs.

The unpowered configuration was tested first: angle of attack sweeps were performed from 0° to 8° at each tunnel speed. For the podded and integrated configurations, the angle of attack was held constant while the propulsor power was varied by setting the fan wheel speed to the values specified in Table 4. In addition to these power sweeps, a number of rake traverses were performed, each at fixed angle of attack and fan wheel speed.

C. Data Collection

1. Force Measurements

The forces and moments on the model were measured using the NASA 843A six-component internal force balance, calibrated at NASA Langley specifically for this test. They are reported in the balance axes system, and rotated to the free-stream axes using the angles of attack measured by an accelerometer mounted on the model near the balance location. The force balance data is taken at 50 Hz over 8 seconds, and each data point is thus an average of 400 samples.

2. Power Measurements

The electrical power drawn by the propulsors is calculated from the continuous reading of voltage, v, and current, i, out of the power supply: $P_E = i\,v$. The electrical power coefficient is then given by its definition (2). The fan wheel speed is determined from the motor controller voltage frequency.

3. Flow Surveys

A rotating rake of 22 stagnation pressure probes was used to survey the flow just upstream of the BLI fan as shown in Figure 12. The rake is driven by a small stepper motor via a timing belt, and the entire rake mechanism is mounted on a strut system attached to the pitch-head behind the model. The foot of the rake contacts the model surface to precisely index its position relative to the model. Force data is not collected while the rake system is in place.

We developed the rake system primarily because the alternative of traversing the flow using a single probe would be too time consuming. The resulting circular sampling window is also appropriate for the round propulsor inflow and outflow. Finally, having the rake contact the model allows for precise positioning of the probes relative to the model even in the presence of model vibration.[i]

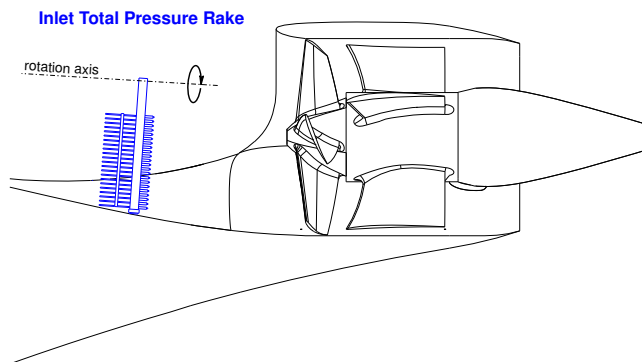[i]A more detailed description of the rake system and flow survey results will be presented in a later paper

Figure 12. Schematic of total pressure rotating rake system for surveying the flow ingested by the integrated configuration propulsor.

American Institute of Aeronautics and Astronautics

D.   Measurement Uncertainty

The instrumentation uncertainties are set by the balance calibration, angle of attack accelerometer, and the instruments on the propulsor power supply, namely

$$\sigma_{F_x} = 0.0975\,\text{lb} \quad, \quad \sigma_{F_z} = 0.3025\,\text{lb} \quad, \quad \sigma_\alpha = 0.005^\circ \quad, \quad \sigma_{P_E} = 0.011\,P_E\;. \tag{6}$$

The uncertainties in free-stream data result from the tunnel calibration and instrumentation, and for $V_\infty = 70$ mph are

$$\sigma_{q_\infty} = 0.0046\,q_\infty \quad, \quad \sigma_{V_\infty} = 0.0022\,V_\infty\;. \tag{7}$$

These instrumentation uncertainties are propagated to the quantities of interest, assuming that all uncertainties are statistically independent, as follows

$$
\begin{aligned}
\sigma_{F_X} &= \left[(\sigma_{F_x} \cos\alpha)^2 + (\sigma_{F_z} \sin\alpha)^2 + (\sigma_\alpha (F_z \cos\alpha - F_x \sin\alpha))^2 \right]^{\frac{1}{2}} \\[4pt]
\sigma_{F_Z} &= \left[(\sigma_{F_x} \sin\alpha)^2 + (\sigma_{F_z} \cos\alpha)^2 + (\sigma_\alpha (F_z \sin\alpha + F_x \cos\alpha))^2 \right]^{\frac{1}{2}} \\[4pt]
\sigma_{C_X} &= \left[\left(\frac{\sigma_{F_X}}{F_X}\right)^2 + \left(\frac{\sigma_{q_\infty}}{q_\infty}\right)^2 \right]^{\frac{1}{2}} C_X \\[4pt]
\sigma_{C_L} &= \left[\left(\frac{\sigma_{F_Z}}{F_Z}\right)^2 + \left(\frac{\sigma_{q_\infty}}{q_\infty}\right)^2 \right]^{\frac{1}{2}} C_L \\[4pt]
\sigma_{P_E}\big|_{C_X=0} &= \left[\left(\frac{\sigma_{P_E}}{P_E}\right)^2 + \left(\frac{\sigma_{F_X}}{P_E}\frac{\mathrm{d}P_E}{\mathrm{d}F_X}\right)^2 \right]^{\frac{1}{2}} P_E \\[4pt]
\sigma_{C_{P_E}} &= \left[\left(\frac{\sigma_{P_E}}{P_E}\right)^2 + \left(\frac{\sigma_{q_\infty}}{q_\infty}\right)^2 + \left(\frac{\sigma_{V_\infty}}{V_\infty}\right)^2 \right]^{\frac{1}{2}} C_{P_E}\;,
\end{aligned}
$$

with the final uncertainties in the quantities of interest given in Table 5.

The metric of interest for this study is the saving in power coefficient, C_{P_E}, due to BLI at the $C_X = 0$ condition. Therefore, the uncertainty in BLI benefit, defined by equation (5), is the result of uncertainty in both measured power and measured stream-wise force. The uncertainty in cruise BLI benefit presented in this study is 2.3%.

Table 5.   **Uncertainty on measured data at $V_\infty = 70$ mph, $\alpha = 2^\circ$. *percent of unpowered configuration C_X.**

Parameter	Value	Percentage
σ_{C_X}	0.00072	2.09*
σ_{C_L}	0.0037	0.58
$\sigma_{C_{P_E}|C_X=0}$	0.0017	2.33

E.   Repeatability

We are careful to differentiate between theoretical *uncertainty*, which is inherited from the specifics of the instrumentation, and *repeatability*, which is the actual spread in measurements taken at the same condition.

To quantify the repeatability, we proceed as follows. A polynomial curve-fit is applied to data taken during a given run, namely an angle of attack sweep (at given tunnel speed) or power sweep (at given angle of attack and tunnel speed). A function standard deviation, σ, of all the polynomial curve-fits for the same run conditions is then analytically computed. Repeatability is quoted as the 95% confidence interval $1.96\,\sigma$, and identified as Δ.

During the wind tunnel test campaign, data was taken for a number of runs at the same conditions. These runs were spread throughout the four weeks of tests, and we took as many similar runs as time allowed. For all quantities of interest, repeatability is found to be within the uncertainty bounds.

VI.   Aerodynamic Characteristics and BLI Benefit

This section presents the measured force coefficients for the three model configurations. Measured power coefficients for the podded and integrated configurations are also presented and compared to determine the aerodynamic BLI benefit in terms of propulsive power. The coefficients and angles of attack shown here have not been corrected for wind tunnel wall effects. The rationale is that the focus of this experiment is on the *differences* between the BLI and non-BLI configurations. Since both configurations have essentially the same aerodynamic far-fields from the lift, volume, etc., they would have the same standard wind tunnel corrections, and any differences in required power would not be affected by the corrections.

A.   Lift, Drag, and Power Characteristics

Figures 13 and 14 show the measured lift coefficients and stream-wise force coefficients versus angle of attack for the three models. The lines give the average for each configuration, and the symbols show different runs.

The lift curves are nearly the same for all three configurations. The slightly higher lift of the podded configuration at large angles of attack can be attributed to the added lift of the podded nacelles. This is not a factor at the lower angles of attack, which is where the cruise condition occurs as described below.

Figure 15 shows the electrical power required by the podded and integrated propulsors versus fan wheel speed, with the different symbols corresponding to different operating points and different runs. The motor controllers are able to hold the wheel speed within 25 rpm ($\Delta U_{\text{tip}}/V_\infty = 0.006$), and repeatability in power level for podded and integrated configurations is $\Delta C_{P_E} = 0.0003$ and 0.0002, respectively. Note that the integrated propulsors require slightly more power for a given fan speed, as expected from the lower average fan-face velocities in the ingested fuselage boundary layer.

B.   BLI Benefit Near Simulated Cruise

We use the term *simulated cruise condition* or simply *cruise condition* to refer to the model condition at $2°$ angle of attack and a power level for which the net stream-wise force is zero. A full-size D8.2 aircraft is designed to fly at a $C_L \simeq 0.7$, which is achieved at an angle of attack of roughly $2°$. Simulated cruise is thus the scale model equivalent of a full-size D8 flying in steady level flight. Figure 13 shows that all three
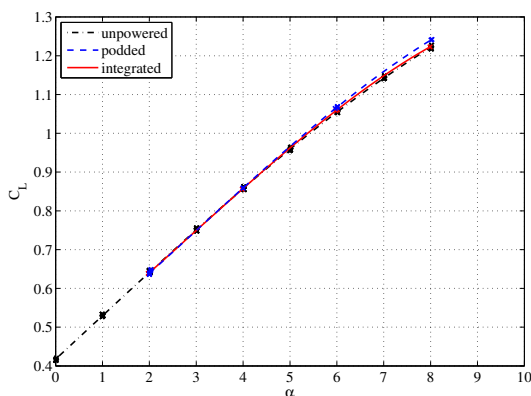

Figure 13.   Lift coefficient versus angle of attack for all three configurations at $V_\infty = 70$ mph. The podded and integrated curves are shown for propulsors at $\Omega = 10\,600$ rpm.   Repeatability is $\Delta C_L = 0.003, 0.005, 0.001$ for unpowered, podded, and integrated configurations respectively.
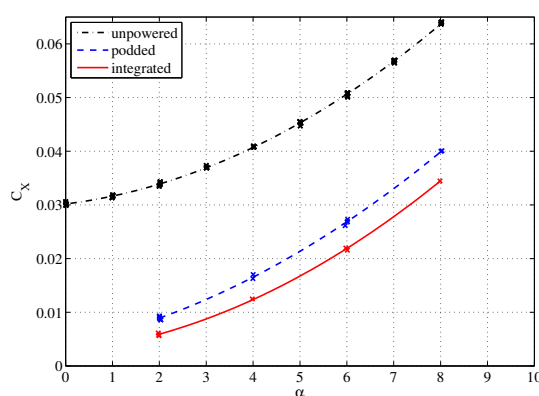

Figure 14.   Net stream-wise force coefficient versus angle of attack for all three configurations at $V_\infty = 70$ mph. The podded and integrated curves are shown for propulsors at $\Omega = 10\,600$ rpm. Repeatability for unpowered, podded, and integrated configurations is $\Delta C_X = 0.0002, 0.0003, 0.0002$.
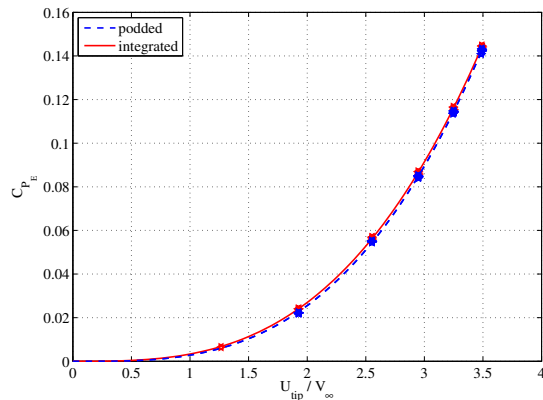
American Institute of Aeronautics and Astronautics

Figure 15. Electrical power versus fan tip speed for $V_\infty = 70$ mph and $\alpha = 2°$ for the podded and integrated configurations, over the whole range used in the experiments. Repeatability is $\Delta C_{P_E} = 0.0003,\ 0.0002$ for podded and integrated configurations, respectively.
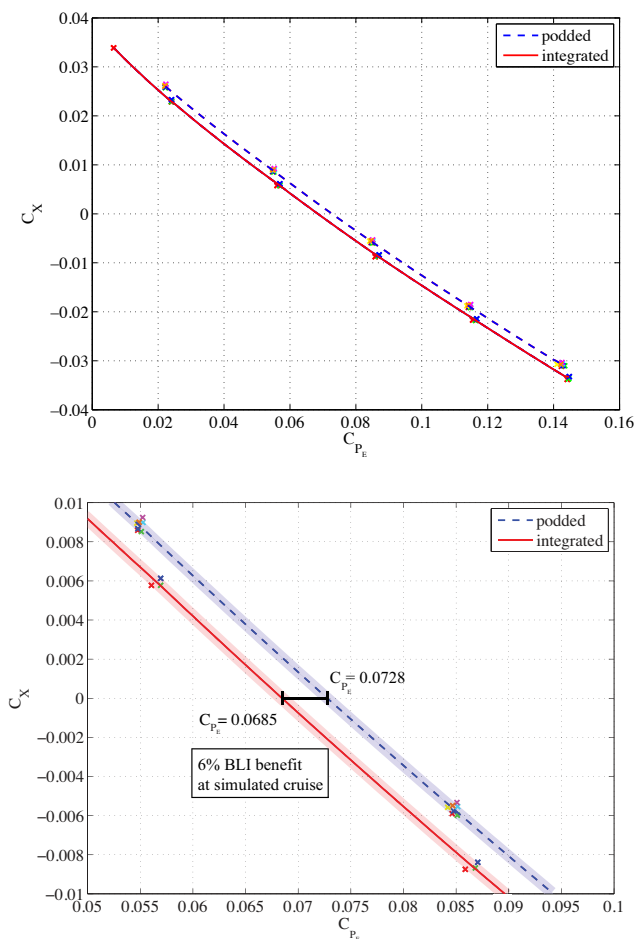

Figure 16. BLI benefit: stream-wise force versus power for $V_\infty = 70$ mph, $\alpha = 2°$ over the whole range measured (top), and closer view near zero net force or simulated cruise (bottom). The shaded regions show the repeatability of $\Delta C_{P_E} = 0.0010$ or equivalently $\Delta C_X = 0.0006$.

American Institute of Aeronautics and Astronautics

configurations have essentially the same lift curve at low angles of attack, so that using α to define the cruise condition is equivalent to using C_L.

Figure 16 shows the net stream-wise force coefficient C_X versus electrical power coefficient C_{P_E} for a range of fan wheel speeds, for both the podded and integrated configurations at $\alpha = 2°$, $V_\infty = 70$ mph. Each cross symbol corresponds to one tunnel run, and the lines give the average between all similar runs. The repeatability is $\Delta C_X = \pm 0.0006$, or equivalently $\Delta C_{P_E} = \pm 0.0010$.

The integrated configuration is seen to require less power, about 0.0043 in C_{P_E}, across the whole range of power levels tested. At simulated cruise ($C_X = 0$) this represents 6.0% less power, which is the measured aerodynamic BLI benefit at simulated cruise.

We must stress that this power saving measurement is for the *electrical* power to the motors. Motor and fan performance experiments needed to convert this to the more relevant propulsor flow power saving were underway at the time this preliminary paper was written, and flow-power results will be reported in a follow-up paper. However, initial results from the motor and fan tests indicated that the motor and fan are operating near peak efficiencies for both configurations, so the current BLI benefit result is not expected to change significantly.

We have also examined the possible effect of the pylons which attach the nacelles to the fuselage in the podded configuration. Given their structural requirements, the pylons were designed for minimum drag so as to not unduly penalize the podded configuration and artificially inflate the BLI benefit of the integrated configuration. However, there was concern over possible interference losses from the pylons interacting with the fuselage boundary layer. Drag measurements were therefore performed with the nacelles removed, but the pylons left in place, which is equivalent to the unpowered configuration with the pylons added. There was no measurable difference in the drag between the models with and without the pylons. Hence, pylon drag is not a factor in the measured BLI benefit.

C.   Reynolds Number Effects

To make the results applicable to full-scale aircraft, it is necessary to ensure turbulent flow is present on all model surfaces. Hence, all surface leading edges and fuselage nose had trips, as described in Section IV.

It is also necessary to ensure that the aerodynamic characteristics of the fan blades are "well-behaved", i.e. free from anomalous low Reynolds number effects such as separation bubble losses or massive laminar separation. If such features were present, turbulence in the ingested boundary layers could conceivably reduce the fan blade profile losses in the integrated case, artificially inflating the measured BLI benefit.

Table 6.   Reynolds numbers at the three operating tunnel speeds.

V_∞	Re_c
42 mph	0.34×10^6
56 mph	0.45×10^6
70 mph	0.57×10^6

To determine the Reynolds number effects on the aerodynamic BLI benefit, measurements were taken on the podded and integrated configurations at three different speeds: $V_\infty = 42$ mph, 56 mph, 70 mph. Table 6 gives the corresponding the Reynolds numbers based on reference chord.

1.   Net Force Versus Power

Before looking at the results, it is useful to consider scaling arguments for the Reynolds numbers effects on net stream-wise force. Note that the net force is the result of airframe drag and propulsor thrust (or blade loading),

$$C_X = \underbrace{C_D}_{\text{airframe drag}} - \underbrace{C_T}_{\text{fan blade loading}},$$

both of which change with Reynolds number. Drag C_D and thrust C_T are not independently defined for a coupled airframe-propulsion system such as the one in the integrated configuration, but thinking of each separately is helpful to understand the trends and a useful approximation.

Consider first the airframe drag contribution to C_X. As the Reynolds number increases, the airframe drag coefficient decreases since all the surfaces are tripped and the boundary layers are turbulent. This overall downward shift is illustrated in Figure 17(a), where the changes are exaggerated to show the trends more clearly. The horizontal black dotted line shows the airframe drag coefficient at a certain condition, and the
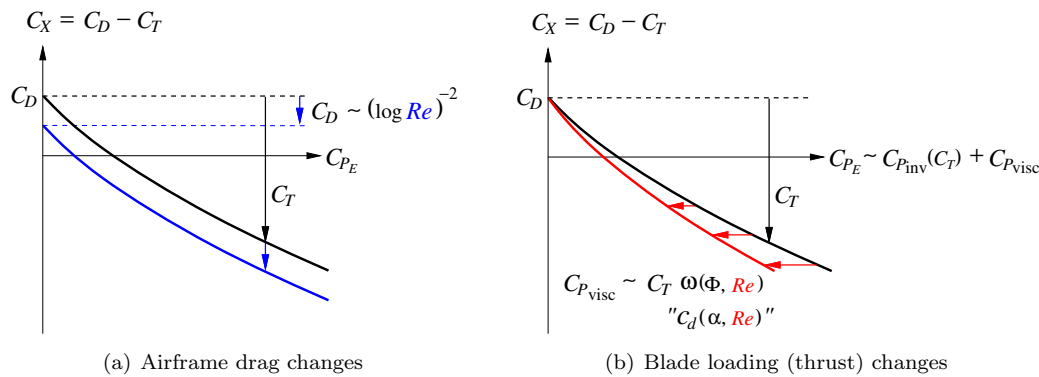
American Institute of Aeronautics and Astronautics

(a) Airframe drag changes

(b) Blade loading (thrust) changes

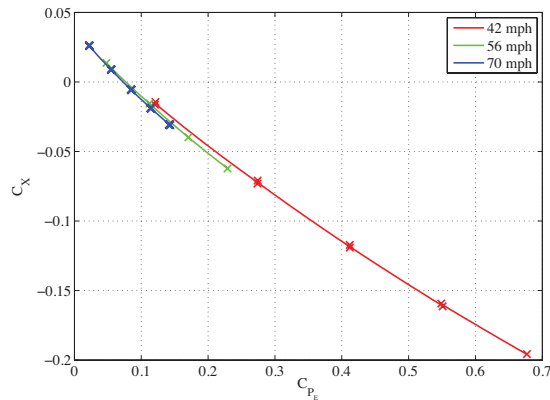**Figure 17. Schematic of the effect of Reynolds number on net force versus power curve, $C_X(C_{P_E})$.**

Figure 18. Force versus power at $\alpha = 2°$ for the integrated configuration at different tunnel velocities $V_\infty = 42, 56, 70$ mph.
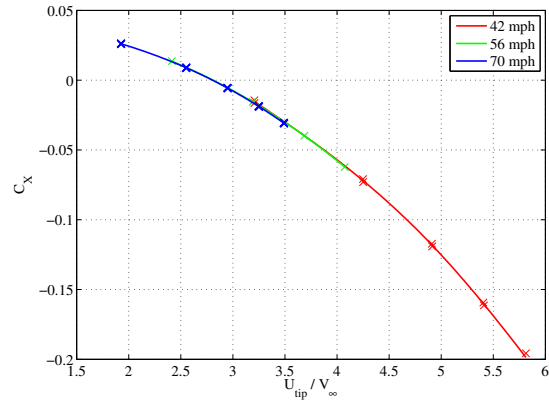
Figure 19. Force versus fan tip speed at $2°$ for the integrated configuration at different tunnel velocities $V_\infty = 42, 56, 70$ mph.

horizontal dotted blue line is the drag coefficient at a higher Reynolds number. The black curve shows the shape of the $C_X(C_{P_E})$ curve at the specific condition, and the change in C_D with Reynolds number shifts this curve downward to the blue curve.

Consider now the thrust contribution to C_X. The power drawn by a fan increases as the blade profile losses increase, and the loss function ω is analogous to the $c_d(\alpha)$ function of an isolated airfoil. With increasing Reynolds number, the fan power and hence C_{P_E} will decrease slightly, with larger changes at higher power levels. This is illustrated in Figure 17(b), in which the $C_X(C_{P_E})$ curve is shown in red for a condition with higher Reynolds number than the black curve, and the shift is larger at larger power levels due to the higher blade loading. Scaling arguments thus imply that Reynolds number effects on airframe drag and on thrust (fan loading) both contribute to shifting the $C_X(C_{P_E})$ curve down and to the left as the Reynolds number is increased.

The measured C_X versus C_{P_E} curves at various Reynolds numbers are shown in Figure 18. The drag coefficient of the airframe (unpowered configuration) at $\alpha = 2°$ was measured to be 0.0339 at $V_\infty = 70$ mph, and its value changes by less than 0.0004 at the other two speeds tested—which is within the measurement uncertainty. Thus, in our $C_X = C_D - C_T$ breakdown, the C_D is unaffected by Reynolds number, and any changes in C_X must stem from changes in C_T. A slight shift is observed in the measured $C_X(C_{P_E})$ curves of Figure 18: this is consistent with high Reynolds number scaling of fan blade losses and is thus an indication that the turbomachinery flow is well-behaved[j].

---

[j]The TF8000 fan was deemed an appropriate choice before the wind tunnel tests were undertaken. Two-dimensional cascade calculations with MISES[8,9] verified that the blades are well-designed for their operating Reynolds number (specifically no undesirable strong separation bubbles). Furthermore, preliminary Navier-Stokes simulations of the internal turbomachinery
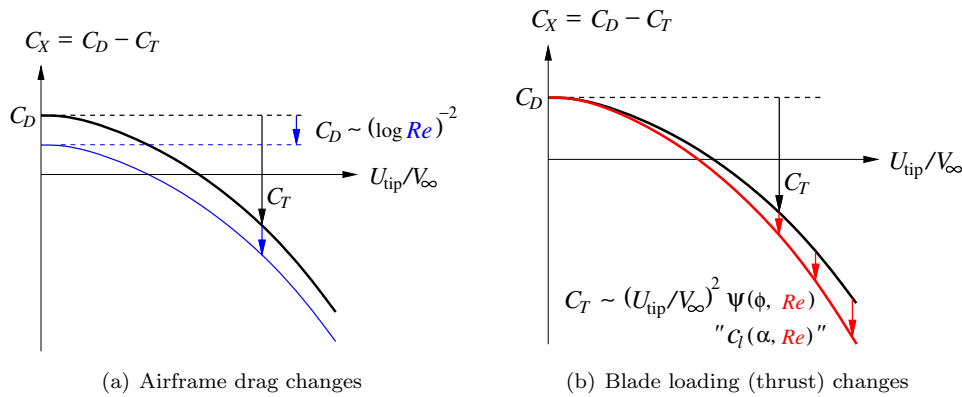
American Institute of Aeronautics and Astronautics

(a) Airframe drag changes   (b) Blade loading (thrust) changes

Figure 20. **Schematic of the effect of Reynolds number on net force versus fan wheel speed curve** $C_X(U_{\text{tip}}/V_\infty)$ **prediction based on scaling arguments.**

2. Net Force Versus Wheel Speed

A similar analysis can be carried out for the changes in net force produced versus wheel speed, and similar conclusions drawn. Consider again the airframe drag and propulsor thrust contributions to net force: $C_X = C_D - C_T$. The change in drag with Reynolds number is expected to be an overall downward shift, as shown in Figure 20(a), in the same way that C_D was expected to decrease at any given power level. Now consider the propulsor thrust contribution to C_X. The fan characteristic is analogous to the $c_\ell(\alpha)$ function of an isolated airfoil: thrust increases slightly with Reynolds number (more negative $-C_T$ values), and larger blade wheel speeds induce larger changes as illustrated in Figure 20(b).

An increase in Reynolds number is thus expected to produce a decrease in C_X, both as a result of decreased drag and increased thrust. The measured net force as a function of wheel speed can be seen in Figure 19 for the three Reynolds numbers considered. Each cross is a separate run at the same conditions, and the lines show the average of all those runs. All the curves collapse, showing that Reynolds numbers are not a factor in the measured stream-wise force. Both the external airframe and internal turbomachinery flows are well-behaved, which is an important condition for the present sub-scale test results to be applicable to a full-size aircraft.

We can draw a second conclusion from Figure 19 by using the fact that the unpowered drag coefficient is unaffected by Reynolds number at $\alpha = 2°$. Given that the overall $C_X = C_D - C_T$ is unchanged as per Figure 19, then the blade loading (thrust) is also insensitive to Reynolds number changes.

Since the observed variations in both the $C_X(U_{\text{tip}}/V_\infty)$ and $C_X(C_{P_E})$ curves with Reynolds number are consistent with well-behaved airframe and fan-blade flows, we conclude that the external flow and the turbomachinery characteristics are free from anomalous low Reynolds number effects. This gives confidence that the low-speed BLI benefit results are applicable to much larger Reynolds numbers.

D. Total Pressure Fields

Surveys of the flow through the propulsors were conducted using the pressure rake system described in Section V.C.3 and Figure 12. The measured contours of total pressure coefficient close to the left and right integrated propulsor inlets can be seen in Figure 21.

A significant finding is the essentially vertical stratification of total pressure at the fan inflow for the $\alpha = 2°$ cruise condition. This is a much more benign distortion than the concentrated vortex cores typically generated by S-duct inlets in buried engine installations, and will produce a nearly sinusoidal unsteady load component on the fan blades.

The inlet distortion shows a larger stream-wise vorticity for the $\alpha = 6°$ case, although still less severe than a fully rolled-up vortex core. This high angle of attack case is however representative of a take-off condition and will typically be accompanied by high power levels (even higher than those of Figure 21) which tend to

---

flow also revealed that the blade chord-wise pressure distribution is well-suited for low Reynolds number operation, from which it was decided that the blades did not require tripping.
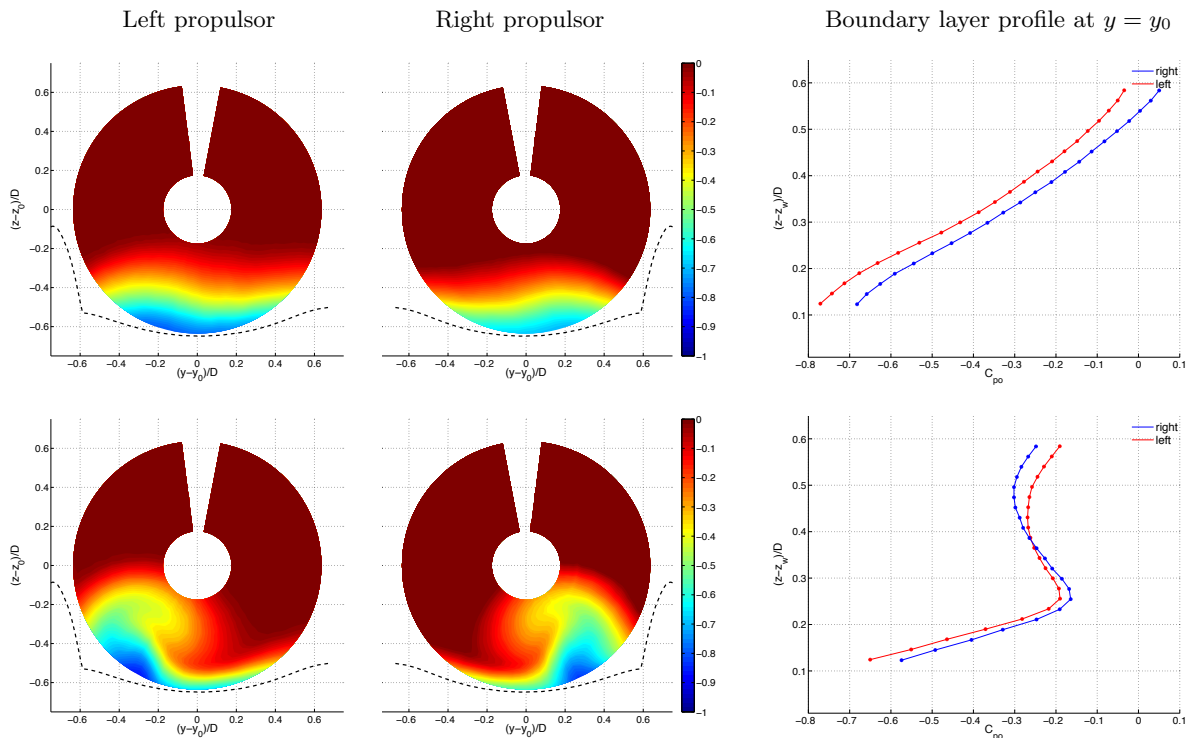
Figure 21. Measured contours of total pressure coefficient just upstream of the integrated propulsor inlets at $\alpha = 2°$, $\Omega = 11\,000\,\mathrm{rpm}$ (top) and at $\alpha = 6°$, $\Omega = 13\,000\,\mathrm{rpm}$ (bottom) with tunnel speed of $V_\infty = 70$ mph.

mitigate cross-flow. The distortion in a realistic flight condition is thus likely to be less severe. Further flow surveys will be conducted in future experiments to include flow angularity measurements and characterize the inlet distortion at additional operating points.

The slight left/right asymmetry in the total pressure profiles of Figure 21 is likely due to the larger power drawn by the right engine, as discussed in next section. The larger mass flow on the right will shifts the loss profile down towards the wall as observed.

E. Power Asymmetry of BLI Propulsors

The propulsors in the podded configuration had symmetrical operating characteristics, requiring the same power for any given fan wheel speed, as can be seen in Figure 22. However, when installed in the integrated configuration, the right propulsor unit required more power than the left, as shown in Figure 23. At the simulated cruise condition ($\alpha = 2°$, $C_X = 0$), the wheel speed is $U_\mathrm{tip}/V_\infty \simeq 2.7$ and the right propulsor requires about 6% more power than the left propulsor[k].

This power asymmetry was observed consistently throughout all integrated configuration tests, and the difference in power required by the right and left propulsors is larger for larger angles of attack: at $6°$ angle of attack and same wheel speed of $U_\mathrm{tip}/V_\infty \simeq 2.7$, the right propulsor requires close to 19% more power than the left one.

Wind-off static thrust measurements confirmed that the power requirement was the same for both propulsors, thus discarding the possibility of hardware malfunction. Furthermore, no signs of airframe asymmetry were observed during the tests on the unpowered configuration. The wind-on power asymmetry must then be due to an asymmetry in the BLI interaction in the integrated configuration, specifically in the fan blade loading, as discussed next.

---

[k]To put this asymmetry in context, if it were created by inlet guide vanes which turned the flow uniformly, the swirl angle would be roughly $3°$.
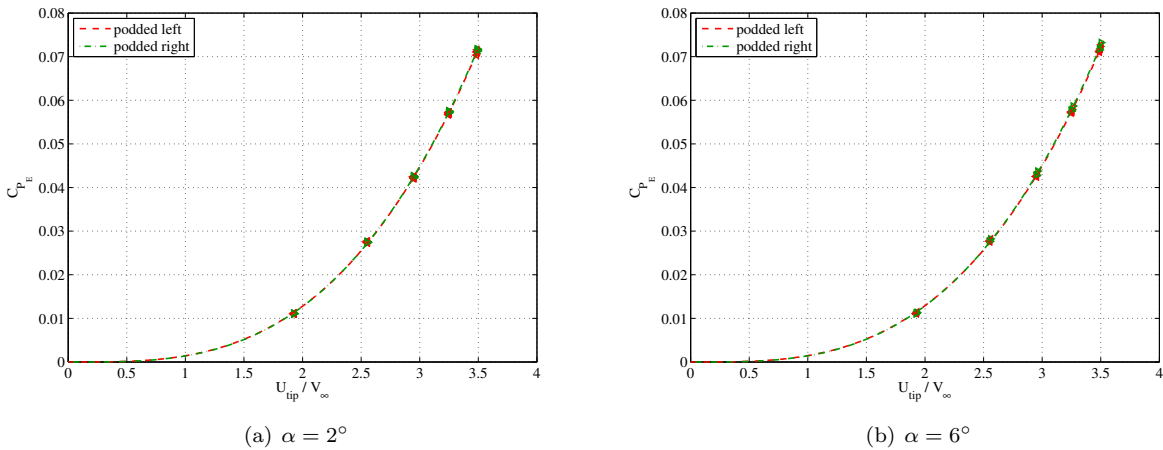
(a) $\alpha = 2°$

(b) $\alpha = 6°$

Figure 22. Power to individual propulsors versus fan speed at $V_\infty = 70$ mph, for $\alpha = 2°$ (left) and $\alpha = 6°$ (right), in the podded configuration: both propulsors require the same power to maintain a given wheel speed.
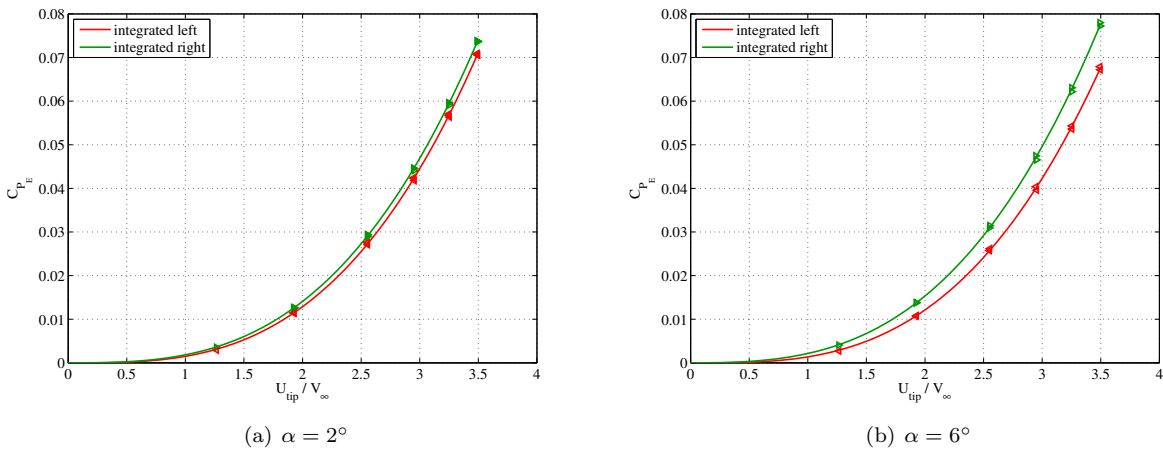

(a) $\alpha = 2°$

(b) $\alpha = 6°$

Figure 23. Power to individual propulsors versus fan speed at $V_\infty = 70$ mph, for $\alpha = 2°$ (left) and $\alpha = 6°$ (right), in the integrated configuration: the right propulsor draws more power than the left.

Blade-loading hypothesis

The power asymmetry is hypothesized to be associated with the cross-flow in the fuselage boundary layers flowing into the fans. The cross-flow was observed in tuft flow visualizations, shown in Figure 24, and is outboard from the fuselage centerline as sketched in the top left of Figure 25. Although the observed cross-flow angles are symmetric with respect to reflection about the aircraft centerline, the two fans have the same right-hand rotation and hence are *anti-symmetric*. This produces an asymmetric interaction between the cross-flow and the fan blades, as sketched in the middle left of Figure 25. The cross-flow velocity V_θ is *co-flowing* for the left fan blades (moving in the same direction as the rotor), and *counter-flowing* for the right fan blades (moving in the opposite direction).

The bottom left of the figure shows the velocity triangles seen by the left and right blades at the bottom 180° position, for the two fans at the same wheel speed—as was the case in the experiments. The right fan's blades see a larger incidence angle as well as a larger relative velocity, so are more highly loaded than the left fan's blades.

The cross-flow angle was observed to increase with angle of attack, as can be seen in the tufts visualization pictures of Figure 24. This would correspond to a larger cross-flow velocity V_θ, and a stronger asymmetry in the blade loading, which is then consistent with the larger measured power asymmetry at $\alpha = 6°$ shown in Figure 23.

American Institute of Aeronautics and Astronautics
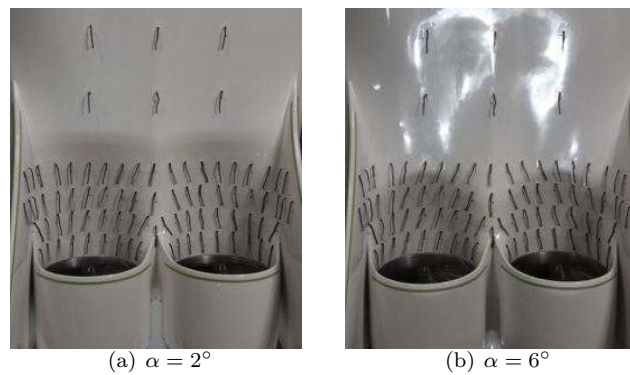
(a) $\alpha = 2°$ (b) $\alpha = 6°$

Figure 24. Tufts flow visualization at $V_\infty = 70$ mph, $\Omega = 12\,250$ showing cross-flow in the fuselage boundary layer upstream of the propulsors: $\alpha = 2°$ (left) and $\alpha = 6°$ (right).
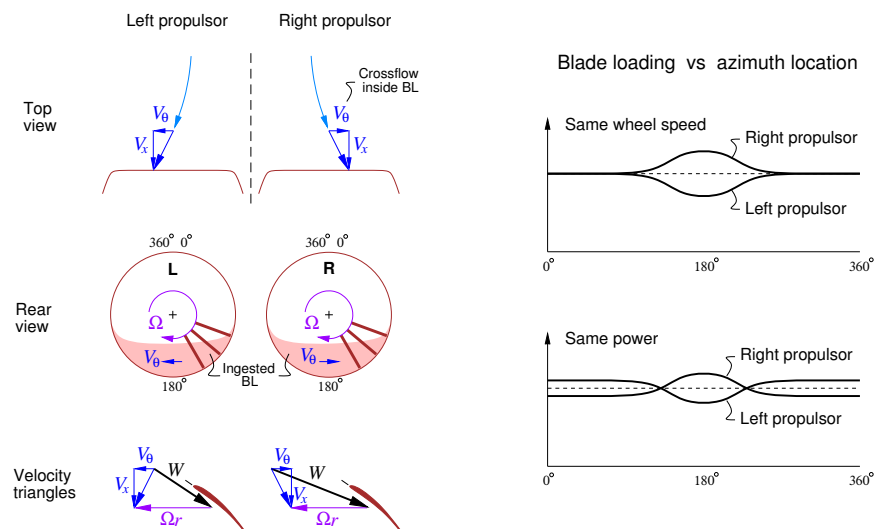

Figure 25. Illustration of cross-flow-induced blade loading differences between left and right propulsors in integrated configuration.

The cross-flow and the resulting loading asymmetry is expected to occur mainly when the blades are immersed in the incoming boundary layer, so that the load versus azimuthal angle on one blade is expected to have the distribution shown on the top right of Figure 25. Averaged over the blade path, the right fan will have a greater torque and extract more power than the left fan.

The left/right power asymmetry is not necessarily as detrimental as it might seem. Although the right motor draws more power, it will also add more power to the flow than the left propulsor, through a basically inviscid shift in fan local operating point. The total power is therefore not influenced by the left/right differences to a first order approximation. However, there will likely be some increased losses because of second order effects, and therefore cause a small reduction in the BLI benefit. Specifically, jet losses increase nonlinearly with power, and also fan blading loss increases away from a minimum-loss design point, which would result in an increase in the total power required to produce a given force.

This can be mitigated by running the two motors at equal power rather than equal wheel speed, which would give the blade loads sketched on the bottom right of Figure 25. This equal-power mode of operation will be used in future experiments, and will likely increase the measured power benefit of the BLI configuration.

Theoretically, a better way to eliminate the power asymmetry is to use counter-rotating fans. These would have the same velocity triangles and hence operate closer to their peak efficiency, thus maximizing the BLI benefit. However, the use of counter-rotating engines in a full-size aircraft is not without significant economic drawbacks.

American Institute of Aeronautics and Astronautics

VII.   Summary and Conclusions

An experimental assessment of the aerodynamic benefit of boundary layer ingestion (BLI) for the twin-engine D8 advanced civil transport has been conducted at the NASA Langley 14×22 Foot Subsonic Wind Tunnel using powered 1:11 scale models. A non-BLI configuration, with propulsors mounted on pylons and ingesting free-stream flow, is used as baseline for assessing the performance of a BLI configuration whose propulsors are flush-mounted on the rear top of the fuselage and ingest roughly 40% of the fuselage boundary layer[1]. The same physical propulsors—each consisting of a fan stage driven by an electric motor—were used for both configurations, with only the tail section (roughly the rear 20%) of the model being different between configurations. The present results thus furnish a first-of-a-kind, back-to-back experimental assessment of the aerodynamic benefits of BLI for a civil aircraft.

The aerodynamic BLI benefit is quantified by the reduction in cruise power, which is a surrogate for fuel burn. The measurements show a 6% saving in electrical power drawn by the BLI model compared to the non-BLI model, with a 95% confidence interval of 2.3% in power. For a full-size D8 aircraft, however, the aerodynamic benefit is only a fraction of the total system-level fuel saving of BLI. It is estimated that the total saving amounts to 15% when including secondary drag and weight reductions enabled by having the engines located on the top rear fuselage. The present experimental results furnish strong support for the feasibility of using BLI to improve the energy efficiency of transport aircraft.

Investigation into the Reynolds number effects on performance shows that with the boundary layer trips employed, the flow around the 13.4 ft span model is in the turbulent regime. Results can thus be scaled to provide information about the BLI benefits for full-size aircraft. The tunnel blockage of the models is only 0.5%, giving small tunnel corrections. Furthermore, these corrections are the same for BLI and non-BLI configurations, and hence the measured BLI benefit is also what would be obtained for vehicles in free air.

With the current D8 model fuselage, there is a left/right symmetric cross-flow, with counter-rotating stream-wise vorticity, in the boundary layer ahead of the propulsors. Because both fans rotate in the same direction, one sees an incoming counter-swirl and the other a co-swirl when the propulsors are mounted on BLI configuration. The two fans thus have operating points roughly 6% different in power input at simulated cruise, but the effect of asymmetry on the total power required is expected to be only minor.

Electrical propulsor power is used in the present work to quantify the BLI benefit, rather than the more appropriate flow mechanical power. The former is the data that has been reduced at present, and this is the main reason for the appearance of the word preliminary in the title. The high degree of commonality between BLI and non-BLI configurations with regards to fuselage and propulsion system parts, and knowing that the motors and fans operate close to peak efficiencies, imply to us that the electrical power measurements are a useful representation of the aerodynamic power differences between non-BLI and BLI aircraft.

Work is underway to translate the electrical power benefit value into flow power, as well as to further interrogate the aircraft flow features experimentally and through CFD. We are also planning additional NASA Langley wind tunnel experiments focused on increasing aerodynamic benefits through redesign of the boundary layer ingesting airframe, for which the accompanying paper[3] gives some initial insight. Future experiments will also target uncertainty reduction via higher tunnel speeds, and will assess aircraft performance at conditions other than cruise.

Acknowledgments

---

[1]as computed based on total fuselage kinetic energy defect in the complementary CFD study[3]

American Institute of Aeronautics and Astronautics

Finally, we are most appreciative of the strong interest, support, and useful input that has been contributed by the NASA Fixed Wing Project management.

References

[1]Greitzer, E., Bonnefoy, P., De la Rosa Blanco, E., Dorbian, C., Drela, M., Hall, D., Hansman, R., Hileman, J., Liebeck, R.H. andLovegren, J., Mody, P., Pertuze, J., Sato, S., Spakovszky, Z., Tan, C., Hollman, J., Duda, J., Fitzgerald, N., Houghton, J., Kerrebrock, J., Kiwada, G., Kordonowy, D., Parrish, J., Tylko, J., Wen, E., and Lord, J., "N+3 Aircraft Concept Designs and Trade Studies, Final Report," *NASA CR 2010-216794*, 2010.

[2]Drela, M., "Development of the D8 Transport Configuration," *29th AIAA Applied Aerodynamics Conference, Honolulu, HI, 27-30 June 2011, AIAA 2011-3970*, 2011.

[3]Pandya, S., Huang, A., Espitia, A., and Uranga, A., "Computational Assessment of the Boundary Layer Ingesting Nacelle Design of the D8 Aircraft," *52nd AIAA Aerospace Sciences Meeting, National Harbor, MD, 13-17 Jan. 2014, AIAA 2014-0907*, 2014.

[4]Betz, A., *Introduction to the Theory of Flow Machines, First English Edition*, Pergamon Press, New York, 1966.

[5]Smith, L., "Wake Ingestion Propulsion Benefit," *Journal of Propulsion and Power*, Vol. 9, No. 1, Jan–Feb 1993, pp. 74–82.

[6]Drela, M., "Power Balance in Aerodynamic Flows," *AIAA Journal*, Vol. 47, No. 7, 2009, pp. 1761–1771.

[7]Gentry, Jr., G. L., Quinto, P. F., Gatlin, G. M., and Applin, Z. T., "The Langley 14- by 22-Foot Subsonic Tunnel: Description, Flow Characteristics, and Guide for Users," Technical Paper 3008, NASA, 1990.

[8]Youngren, H. and Drela, M., "Viscous/Inviscid Method for Preliminary Design of Transonic Cascades," AIAA Paper 91-2364, June 1991.

[9]Youngren, H., "Analysis and Design of Transonic Cascades with Splitter Vanes," Report 203, MIT Gas Turbine Laboratory, Cambridge, MA, 1991.